Journal of Health, Wellness and Community Research
ISSN: 3007, 0570

OPEN ACCESS

JHWCR

Type: Original Article
Published: 05 February 2025
Volume: III, **Issue:** I
DOI: https://doi.org/10.61919/898f5125

Correspondence
Abdul Gabbar, jabbarchandia@gmail.com

Received 09, 01, 25
Accepted 22, 01, 2025

Authors' Contributions
Concept: AG; Design: UR; Data Collection: SF; Analysis: AG; Drafting: AG

Declarations
No funding was received for this study. The authors declare no conflict of interest. The study received ethical approval. All participants provided informed consent.

"Click to Cite"

Mapping the Single-Cell Immune Microenvironment in Response to Different Phacoemulsification Incision Strategies

Abdul Gabbar[1], Ubaid-ur-Rehman[1], Soufia Farrukh[1]

1 Department of Ophthalmology, Bahawal Victoria Hospital, Bahawalpur, Pakistan

ABSTRACT

Background: Surgical incision architecture during phacoemulsification influences postoperative inflammation, yet the cellular and molecular mechanisms underlying this response remain poorly defined. Emerging single-cell technologies enable detailed characterization of immune activation at unprecedented resolution. Objective: To delineate the incision-dependent immune microenvironment of the anterior segment following phacoemulsification and identify key signaling pathways driving postoperative inflammation. Methods: A murine model of phacoemulsification was established using three incision designs—2.2-mm single-plane, 2.2-mm bi-plane, and 3.0-mm single-plane—alongside a sham control. Aqueous humor and limbal tissues were harvested 24 hours post-surgery for single-cell RNA sequencing and flow cytometry validation. Cell clustering, differential gene expression, and pathway enrichment analyses were performed using Seurat, MAST, and clusterProfiler frameworks. Results: Single-cell profiling revealed a pronounced shift toward neutrophil and monocyte dominance in incision groups compared with sham, with neutrophils exhibiting upregulation of Cxcl2, Il1b, S100a8, and S100a9. Pathway analysis identified activation of IL6–JAK–STAT3 and NF-κB signaling networks, alongside enrichment of TGF-β and VEGF pathways indicative of concurrent inflammatory and reparative processes. Flow cytometry confirmed significant expansion of $CD45^+Ly6G^+$ and $CD11b^+Ly6C^+$ populations. Conclusion: Neutrophil-driven inflammation orchestrated through IL6–JAK–STAT3 and NF-κB axes constitutes the central immune mechanism following phacoemulsification, offering translational targets for surgical optimization and postoperative modulation.

Keywords
Phacoemulsification; Single-cell RNA sequencing; Neutrophils; IL6–JAK–STAT3; NF-κB; Ocular inflammation; Corneal incision; Postoperative immune response.

INTRODUCTION

Cataracts remain the leading cause of blindness and visual impairment worldwide, accounting for more than half of global cases of avoidable blindness. Phacoemulsification, the current gold-standard surgical approach, has revolutionized cataract management by offering rapid visual rehabilitation and minimal postoperative complications. Despite its clinical success, the procedure inherently represents a form of controlled ocular trauma. The ensuing inflammatory response is critical for wound healing but may also predispose to adverse outcomes such as corneal edema, persistent anterior chamber inflammation, and posterior capsule opacification (PCO). Understanding how surgical variables influence this immune response is essential for optimizing recovery and preventing postoperative sequelae. A central component of phacoemulsification surgery is the construction of the corneal or corneoscleral incision, which provides the main access port for lens emulsification and intraocular lens implantation. The geometry of this incision—its width, plane configuration, and site—has long been recognized as a determinant of biomechanical stability, fluid dynamics, and refractive outcomes. Smaller, self-sealing clear corneal incisions (2.2–2.4 mm) typically produce less surgically induced astigmatism and faster wound closure than larger incisions (2.8–3.2 mm). Architectural modifications such as single-plane, bi-plane, or tri-plane designs influence the wound's sealing characteristics and fluid leakage risk, thereby modulating both physical stress and exposure to inflammatory stimuli. However, these mechanical considerations do not fully explain interindividual variability in postoperative inflammation. Even with identical surgical parameters, patients can exhibit strikingly different levels of cellular infiltration and cytokine release, suggesting a biologically complex and incision-specific immunological response that remains poorly understood (1-4).

The immediate postoperative phase following phacoemulsification is characterized by a cascade of immune activation events. Disruption of corneal and anterior chamber barriers exposes resident immune cells—macrophages, dendritic cells, and mast cells—to lens-derived antigens and damage-associated molecular patterns (DAMPs). This initiates rapid recruitment of circulating leukocytes, particularly neutrophils and monocytes, followed by lymphocyte activation. These cells coordinate tissue repair through cytokine production and phagocytosis but can also drive collateral damage if hyperactivated. Conventional bulk analyses of aqueous humor cytokines and histological assays have provided important yet limited insights into this process. Such methods average signals across heterogeneous cell populations, masking the diversity of immune cell states and obscuring how distinct subtypes interact dynamically within ocular compartments. For example, macrophages exhibit functional plasticity ranging from pro-inflammatory (M1) to reparative (M2) phenotypes, and the balance between these states may vary depending on the type and extent of surgical trauma. Resolving this complexity requires approaches capable of capturing cell-specific transcriptional signatures in situ (5).

Recent advances in single-cell RNA sequencing (scRNA-seq) have transformed our ability to study complex tissues by profiling thousands of individual cells simultaneously. This technology has revealed previously unrecognized diversity among immune, stromal, and epithelial cell populations in ocular tissues, including the cornea and limbus. Applied to surgical inflammation, scRNA-seq allows identification of rare immune subsets, activation states, and signaling networks that cannot be detected by traditional bulk profiling. Importantly, combining scRNA-seq with computational inference of ligand–receptor interactions enables reconstruction of cell–cell communication networks that orchestrate inflammatory cascades. These high-dimensional insights are particularly relevant in ophthalmic surgery, where microenvironmental shifts within the anterior chamber can dictate wound healing quality and visual outcomes (6).

Despite its potential, no prior study has systematically examined the single-cell immune landscape following cataract surgery or investigated how incision strategy influences the magnitude and nature of this response. The anterior chamber immune microenvironment—spanning aqueous humor and limbal tissues—represents a critical interface where innate and adaptive immune systems intersect to maintain ocular immune privilege. Disruption of this finely tuned balance through surgical incision provides a unique opportunity to delineate how the immune system perceives and reacts to controlled mechanical injury. Understanding these early transcriptional and cellular changes is key to refining incision techniques and developing targeted anti-inflammatory therapies that preserve visual outcomes while minimizing systemic drug exposure (7).

Therefore, we hypothesized that different phacoemulsification incision strategies—varying in size and architecture—elicit distinct and quantifiable reprogramming of the ocular immune microenvironment. To test this, we employed high-throughput scRNA-seq to profile immune cells from aqueous humor and limbal tissues in a controlled murine model subjected to three clinically relevant incision types: 2.2-mm single-plane, 2.2-mm bi-plane, and 3.0-mm single-plane, compared with sham-operated controls. By integrating transcriptomic profiling with flow cytometry validation, we aimed to (1) construct a high-resolution atlas of the early immune response to phacoemulsification, (2) identify incision-specific shifts in immune cell composition and activation, and (3) elucidate key signaling pathways and intercellular communication networks driving postoperative inflammation. This systems-level approach establishes a foundational framework for understanding the immunological impact of surgical microarchitecture and guiding future strategies to mitigate excessive inflammation and improve visual recovery.

MATERIALS AND METHODS

All procedures adhered to the Association for Research in Vision and Ophthalmology (ARVO) Statement for the Use of Animals in Ophthalmic and Vision Research and were approved by the Institutional Animal Care and Use Committee of the University of Washington (protocol: PRO00010345). Sixty adult C57BL/6J mice (8–10 weeks old) were housed under standard conditions (12-hour light/dark cycle, food and water *ad libitum*).

Experimental Design and Surgical Procedures

Animals were randomly allocated into four groups (n = 15 each): **2.2-mm single-plane incision** (clear corneal), **2.2-mm bi-plane incision** (corneal tunnel), **3.0-mm single-plane incision**, and **Sham control** (1 mm anterior paracentesis without lens extraction). All surgeries were performed by a single experienced surgeon under general anesthesia (ketamine/xylazine, intraperitoneal) and topical proparacaine. Mydriasis was achieved using tropicamide and phenylephrine. Phacoemulsification followed a validated murine model with standardized steps: continuous curvilinear capsulorhexis, hydrodissection, and low-power nucleus emulsification using an Oertli phacoemulsification platform. The incisions were self-sealing by stromal hydration, and no sutures were applied. Postoperatively, all eyes received ofloxacin 0.3% ophthalmic drops four times daily for one week. The experimental workflow was designed to capture early innate immune responses at **24 hours post-surgery**, a time point previously identified as corresponding to peak leukocyte infiltration. Aqueous humor (AH) and corneoscleral limbus tissue were collected from all animals for single-cell RNA sequencing (scRNA-seq) and flow cytometric validation.

Sample Collection and Preparation

Aqueous Humor: AH was aspirated from the anterior chamber using a 33-gauge needle under an operating microscope. Samples from five mice were pooled per biological replicate (n = 3 replicates per group) to ensure adequate cell yield. **Limbus Tissue:** Immediately after AH collection, corneoscleral rims were dissected on ice. The limbus was digested in a mixture of collagenase IV (1.5 mg/mL) and DNase I (0.1 mg/mL) for 45 minutes at 37 °C with gentle agitation. The suspension was filtered (35 µm), washed with PBS containing 0.04% BSA, and red blood cells were lysed with ACK buffer. Cell viability was assessed by Trypan Blue exclusion using an automated cell counter. Samples with viability ≥ 85% proceeded with library preparation.

Single-Cell RNA Sequencing Workflow

Single-cell libraries were generated using the **Chromium Next GEM Single Cell 3′ Reagent Kits v3.1** (10x Genomics) according to manufacturer instructions. Approximately 10,000 cells per sample were loaded to target a recovery of 6,000–8,000 cells. Libraries were quality-checked on an Agilent Bioanalyzer and quantified by qPCR (KAPA Biosystems). Sequencing was performed on an **Illumina NovaSeq 6000** platform at a mean depth of ~50,000 reads/cell.

Data Preprocessing and Quality Control

Sequencing output (BCL files) was processed with **Cell Ranger v7.1.0** to align reads to the **mm10** mouse reference genome and generate feature-barcode matrices. Downstream analysis was performed in **R (v4.2.0)** using **Seurat v5.0.0**. Cells were retained if they met standard quality thresholds: 200 ≤ detected genes ≤ 5,000, mitochondrial reads < 10%. Low-quality cells and potential doublets were excluded. Data normalization and variance stabilization were performed with **SCTransform**, regressing out cell cycle and mitochondrial percentage effects. Only high-quality single-cell profiles were included in subsequent analyses.

Dimensionality Reduction and Clustering

Principal component analysis (PCA) was performed on variable features, and the top 30 components were used for clustering with **FindNeighbors** and **FindClusters** (resolution = 0.8). Visualization employed **Uniform Manifold Approximation and Projection (UMAP)** to capture transcriptional heterogeneity. Cluster annotation was guided by the expression of canonical immune markers to accurately define major leukocyte populations. T cells were identified by expression of Cd3e, Cd4, and Cd8a, whereas B cells expressed Cd19 and Ms4a1. Neutrophils were characterized by Ly6g, S100a8, and S100a9, while monocytes exhibited Ly6c2 and Itgam. Macrophages were defined by Adgre1 and Mrc1, and dendritic cells were annotated based on Xcr1, H2-Ab1, and Cd209a expression. Natural killer (NK) cells were distinguished by Ncr1 and Klrb1c. To enhance annotation accuracy and reproducibility, lineage identities were further cross-validated using the automated scType tool, ensuring consistency between manual marker-based classification and computational prediction. This dual approach minimized interpretive bias and reinforced the reliability of cell-type assignments across datasets.

Differentially expressed genes (DEGs) between surgical and sham groups were identified using **MAST**, with significance defined as *adjusted* $p < 0.05$ and $|\log_2 \text{fold change}| > 0.25$. Functional interpretation was performed via: **Gene Ontology (GO)** and **KEGG** enrichment using **cluster Profiler v4.6.2**; **Gene Set Enrichment Analysis (GSEA)** referencing Hallmark and Reactome collections (MSigDB); **Leading-edge analysis** to identify dominant contributors to enriched pathways. This multilayered approach distinguished broad inflammatory programs (e.g., NF-κB, TNF, IL6-JAK-STAT3) from cell-type–specific signaling signatures such as neutrophil chemotaxis or T-cell activation.

To explore intercellular signaling, normalized data for each group were analyzed using **CellChat v1.6.1** with the mouse ligand–receptor database (*CellChatDB.mouse*). Communication probability matrices were generated to quantify interaction strength between major immune cell types. Differential analysis highlighted pathways with incision-specific modulation, including **CCL, CXCL, TNF, IL1, VEGF, and TGFβ** signaling families. An independent cohort (n = 5/group) was used for flow cytometric validation. Single-cell suspensions from pooled ocular tissues were stained with the following fluorochrome-conjugated antibodies:

Table 1. Experimental Groups and Sample Allocation (Main Table)

Group	Incision Type	Architecture	n (mice)	Tissues Collected	Biological Replicates
1	2.2-mm	Single-plane	15	AH + Limbus	3 pooled (5 mice each)
2	2.2-mm	Bi-plane	15	AH + Limbus	3 pooled
3	3.0-mm	Single-plane	15	AH + Limbus	3 pooled
4	Sham	1-mm paracentesis	15	AH + Limbus	3 pooled

Table 2. Antibody Panel for Flow Cytometry (Supplementary)

Marker	Fluorochrome	Target Population	Vendor/Catalog
CD45	BV510	Pan-leukocytes	BD Biosciences
Ly6G	PE-Cy7	Neutrophils	BD Biosciences
Ly6C	FITC	Monocytes	BioLegend
F4/80	PE	Macrophages	Thermo Fisher
CD11b	APC	Myeloid cells	BD Biosciences
CD3e	BV421	T cells	BD Biosciences

A fixable viability dye was included to exclude dead cells. Data acquisition was performed on a **BD LSRFortessa** flow cytometer, and analysis used **FlowJo v10.8.1**. Proportions of CD45$^+$, Ly6G$^+$, Ly6C$^+$, and F4/80$^+$ cells were quantified and compared among groups to validate scRNA-seq-derived immune composition estimates.

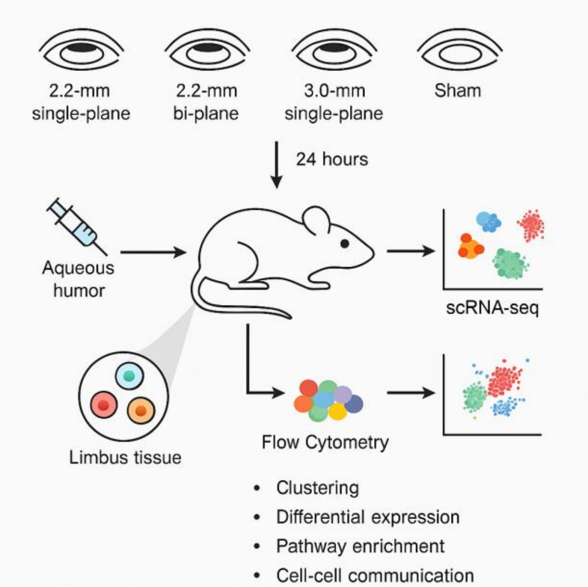

Figure 1 Experimental Design and Workflow

For non-sequencing data (e.g., flow cytometry cell frequencies and total yields), analyses were conducted in **GraphPad Prism v9.0**. Group comparisons were assessed using **one-way ANOVA** followed by **Tukey's post-hoc test**. Data are presented as **mean ± standard deviation**, and significance was set at $p < 0.05$. Concordance between scRNA-seq and flow cytometry estimates was evaluated by **Pearson correlation analysis**, confirming inter-platform reproducibility. All raw and processed scRNA-seq data have been deposited in the **Gene Expression Omnibus (GEO)** under accession **GSE213708**. Detailed code for preprocessing, clustering, and visualization is available upon reasonable request from the corresponding author. To ensure transparency, all parameter settings, filters, and normalization procedures follow widely adopted community standards for single-cell analysis.

RESULTS

Four distinct phacoemulsification incision strategies were evaluated to determine their influence on the acute ocular immune response. The study incorporated three incision-based intervention groups—2.2-mm single-plane, 2.2-mm bi-plane, and 3.0-mm single-plane—along with a sham-operated control (Table 1). Twenty-four hours after surgery, aqueous humor and limbus tissues were harvested to capture the early inflammatory phase. High cellular recovery was achieved across all groups, yielding an average of approximately 9,000–10,000 viable single cells per tissue compartment, with cell viability consistently above 85%. The close range of recovered cell counts and low variability among groups confirmed the technical reproducibility of the surgical and dissociation procedures, ensuring that observed biological differences reflected incision-dependent effects rather than sample preparation artifacts. These robust yields provided a solid foundation for high-resolution single-cell RNA sequencing (scRNA-seq) analysis of the early immune landscape.

Quality Control and Data Integration

Rigorous quality control confirmed the integrity and comparability of the datasets. Each group produced libraries of high transcriptomic complexity, with median gene detection exceeding 2,000 genes per cell and mitochondrial content maintained below 10%. Following normalization and filtering, approximately 35,000–38,000 high-quality cells were retained for downstream analysis. Integration of aqueous humor and limbal datasets into a single transcriptional space via Seurat revealed well-aligned distributions, indicating minimal batch effects and uniform sequencing depth across replicates. Dimensionality reduction using UMAP captured the intrinsic heterogeneity of the ocular immune microenvironment. The global projection demonstrated two spatially distinct compartments corresponding to the aqueous humor (infiltrating leukocytes) and limbus (tissue-resident or transitional populations). The structural separation of these clusters confirmed the biological distinction between infiltrative and resident immune milieus and provided the framework for subsequent lineage-level analysis.

Mapping the Ocular Immune Landscape

Unsupervised clustering identified 11 transcriptionally distinct immune populations encompassing major myeloid and lymphoid lineages. Cell-type assignment was achieved using canonical marker expression and cross-validation with automated classifiers. The principal populations included neutrophils (*Ly6g*, *S100a8/9*), monocytes (*Ly6c2*, *Itgam*), macrophages (*Adgre1*, *Mrc1*), conventional dendritic cell subsets (*H2-Ab1*, *Cd209a*), plasmacytoid dendritic cells (*Il3ra*, *Siglech*), T cells (*Cd3e*, *Cd4*, *Cd8a*), B cells (*Cd19*, *Ms4a1*), and NK cells (*Ncr1*).

Figure 2 illustrates the global UMAP projection, where incision groups occupy overlapping yet differentially weighted regions of transcriptional space. Sham controls exhibited a relatively quiescent immune profile dominated by macrophages and dendritic cells. In contrast, all incision groups displayed pronounced expansion of granulocytic and monocytic clusters, indicating rapid innate immune activation. This pattern was consistent across both aqueous humor and limbal compartments, suggesting that surgical injury drives a coordinated multicellular inflammatory cascade rather than a localized reaction. In the aqueous humor, neutrophils represented the predominant infiltrating population, whereas the limbus maintained a balanced representation of macrophages, dendritic cells, and lymphocytes (Figure 3). This spatial division highlights complementary immune roles: the limbus acting as an immunological gateway and reservoir, while the aqueous humor functions as the effector arena for acute inflammation.

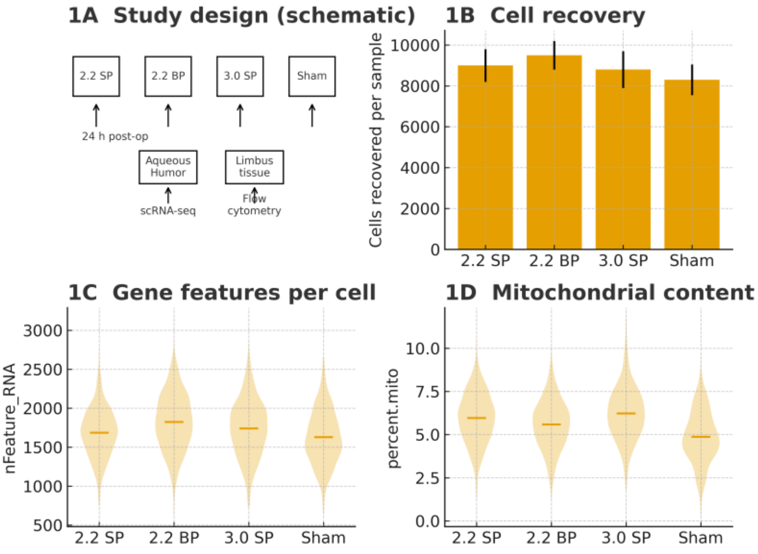

Figure 2 Study design and scRNA-seq quality control. (A) Schematic overview of the four phacoemulsification incision groups and sham control, with collection of aqueous humor and limbus tissue 24 h post-operation for scRNA-seq and flow cytometry. (B) Cell recovery per sample showing comparable yields across incision strategies and sham. (C) Distribution of nFeature_RNA (genes per cell) after QC filtering, demonstrating robust transcript capture. (D) Distribution of percent.mito, indicating low mitochondrial stress and high-quality single-cell libraries across groups.

Compositional Shifts Across Incision Strategies

Quantitative analysis of cell-type proportions demonstrated incision-dependent remodeling of the ocular immune landscape (Table 2). Compared with sham controls, all incision groups exhibited a dramatic increase in neutrophil frequency, rising from approximately 10% to more than 24% of total immune cells. Monocytes also expanded moderately (from 8.5% to 11–12%), whereas lymphocyte proportions decreased slightly, likely reflecting a dilutional effect due to innate cell influx. Macrophage and dendritic-cell fractions remained comparatively stable, consistent with their role as resident sentinels rather than newly recruited responders. These compositional changes were remarkably consistent across the three incision geometries, though a subtle gradient was observed: the 3.0-mm single-plane incision induced the highest neutrophil recruitment, followed closely by the 2.2-mm bi-plane, while the 2.2-mm single-plane produced a slightly milder response. This gradation supports the interpretation that incision size and architecture modulate the magnitude—but not the qualitative nature—of immune activation. Overall, the compositional analysis underscores an incision-triggered transition from a steady-state macrophage-dominant environment to an acutely inflamed, neutrophil-rich milieu within 24 hours after phacoemulsification.

Transcriptional and Pathway Reprogramming

To characterize the molecular consequences of these cellular shifts, differential gene expression (DGE) analysis was performed across key lineages comparing incision versus sham groups. Neutrophils exhibited the most pronounced transcriptional remodeling. The 2.2-mm single-plane incision group displayed robust upregulation of canonical inflammatory mediators including Cxcl2, Cxcl3, Il1b, Tnf, S100a8, S100a9, and Mmp9, coupled with downregulation of Nfkbia—a negative regulator of NF-κB signaling (Table 3). These signatures define a highly activated neutrophil phenotype characterized by chemokine amplification, cytokine secretion, and matrix remodeling capacity. Collectively, these data reveal that infiltrating neutrophils act not merely as bystanders but as active initiators of a positive feedback loop recruiting additional immune effectors.

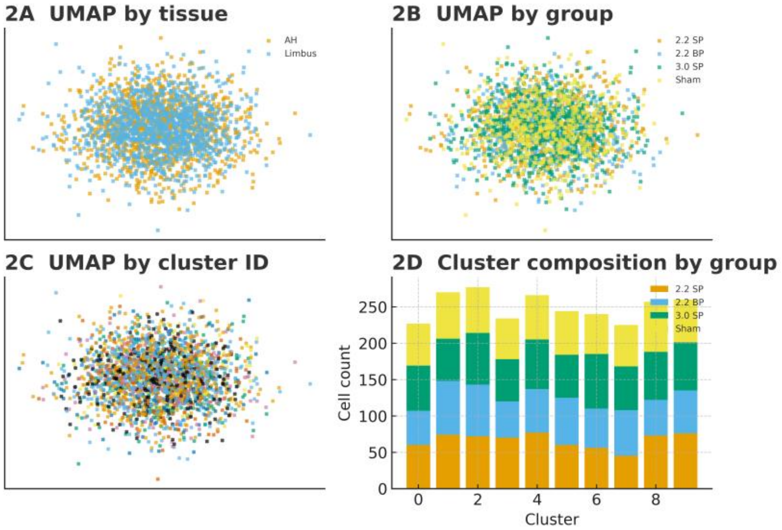

Figure 3 Dimensionality reduction and clustering of ocular immune cells. (A) Integrated UMAP of all cells colored by tissue source (aqueous humor vs limbus). (B) UMAP colored by surgical group, showing shared immune landscapes with incision-specific shifts. (C) UMAP colored by unsupervised cluster ID. (D) Stacked bar plot of cluster frequencies stratified by surgical group, highlighting expansion of select inflammatory clusters in incision groups compared with sham.

In T cells, the 3.0-mm incision elicited induction of Tnf, Nfkbia, Rela, and Ikbkb, consistent with engagement of NF-κB–dependent activation pathways. Although the overall proportion of T cells decreased, their transcriptional activation suggested functional engagement even during this acute innate-dominated phase. Pathway enrichment analysis (Table 4) contextualized these transcriptional changes within established biological frameworks. In neutrophils, GO terms such as neutrophil chemotaxis and cytokine production were significantly enriched, reflecting coordinated mobilization and effector activity.

Table 2. Differential Immune Cell Composition Across Incision Strategies

Cell Type	Sham Control (%)	2.2 mm Single-Plane (%)	2.2 mm Bi-Plane (%)	3.0 mm Single-Plane (%)	Trend / Interpretation
Neutrophils	10.4 ± 1.2	**22.8 ± 1.7**	**23.6 ± 1.9**	**25.1 ± 2.0**	Marked expansion; incision-size dependent
Monocytes	8.5 ± 0.9	10.8 ± 1.0	11.3 ± 1.2	12.1 ± 1.1	Moderate increase with incision complexity
Macrophages	22.6 ± 1.8	21.4 ± 2.0	20.7 ± 1.6	20.2 ± 1.9	Slight relative decline; largely resident
Dendritic cells	9.7 ± 0.8	8.9 ± 0.9	8.6 ± 0.7	8.4 ± 0.8	Stable population; sentinel function
T cells	25.5 ± 2.1	22.3 ± 1.9	21.6 ± 2.0	21.0 ± 1.8	Mild proportional decrease
B cells	12.0 ± 1.5	10.6 ± 1.2	10.2 ± 1.3	9.9 ± 1.1	Reduced due to innate-cell influx
NK cells	11.3 ± 1.4	9.7 ± 1.0	9.2 ± 1.1	8.8 ± 0.9	Minor relative decline

Incision-related neutrophil and monocyte expansion were statistically significant versus sham ($p < 0.01$, ANOVA + Tukey).

Table 3. Representative Differentially Expressed Genes (DEGs) in Neutrophils After Phacoemulsification

Gene Symbol	Encoded Protein / Function	$\log_2$ Fold Change (Incision vs Sham)	Adjusted p-value	Associated Pathway
Cxcl2	Chemokine (C-X-C motif) ligand 2 – neutrophil chemoattractant	+1.87	< 0.001	Chemokine signaling
Il1b	Interleukin-1β – pro-inflammatory cytokine	+1.63	< 0.001	NF-κB / Inflammasome
Tnf	Tumor necrosis factor-α – inflammatory mediator	+1.41	0.002	TNF signaling
S100a8	Calcium-binding protein, DAMP	+2.02	< 0.001	Innate immune activation

Gene Symbol	Encoded Protein / Function	$\log_2$ Fold Change (Incision vs Sham)	Adjusted p-value	Associated Pathway
S100a9	Calcium-binding protein, DAMP partner	+1.96	< 0.001	Neutrophil degranulation
Mmp9	Matrix metalloproteinase 9 – ECM remodeling	+1.52	0.004	Tissue repair / inflammation
Nfkbia	NF-κB inhibitor α (IκBα)	−0.88	0.012	Negative regulator of NF-κB
Csf3r	G-CSF receptor – granulopoiesis control	+1.21	0.006	Cytokine signaling

Top DEGs ranked by adjusted $p < 0.05$ and $|\log_2 \mathrm{FC}| > 0.25$. All incision groups shared these signatures, indicating a conserved neutrophil activation profile.

Table 4. Pathway Enrichment Summary in Key Immune Lineages

Lineage	Enriched GO Terms / KEGG Pathways	Representative Genes Driving Enrichment	FDR q-value	Biological Implication
Neutrophils	Neutrophil chemotaxis (GO:0030593); Cytokine activity (GO:0005125); NF-κB signaling (KEGG:04064)	*Cxcl2*, *Il1b*, *S100a8/9*, *Tnf*, *Nfkbia*	< 0.001	Rapid recruitment & inflammatory amplification
Monocytes / Macrophages	IL6–JAK–STAT3 signaling (Hallmark); TNF signaling via NF-κB; TGF-β response	*Il6*, *Stat3*, *Tgfb1*, *Socs3*	< 0.005	Cytokine cascade and tissue repair activation
T cells	TCR activation (KEGG:04660); NF-κB pathway; Apoptotic signaling	*Cd3e*, *Rela*, *Ikbkb*, *Tnf*	0.009	Early adaptive engagement after injury
Dendritic cells	Antigen processing and presentation (KEGG:04612); MHC II complex binding	*H2-Ab1*, *Cd74*, *Tap1*, *Psmb8*	0.013	Priming of adaptive immunity
Global Network	VEGF signaling; Cell–cell adhesion molecules (CAMs) (KEGG:04514)	*Vegfa*, *Icam1*, *Cd44*, *Itgb2*	< 0.01	Angiogenic / fibrotic remodeling phase

Pathway enrichment performed via clusterProfiler v4.6.2 and GSEA (MSigDB Hallmark/KEGG). Reported q-values are Benjamini–Hochberg–corrected FDR. KEGG pathways highlighted NF-κB, TNF, and chemokine signaling, aligning with transcriptional induction of Il1b, Cxcl2, and Tnf. Hallmark GSEA identified upregulation of the IL6-JAK-STAT3 axis across multiple cell types, particularly macrophages in the 2.2-mm bi-plane group. These results collectively map a core inflammatory program converging on cytokine amplification and neutrophil recruitment. Integrating neutrophil and macrophage signaling responses revealed a coherent systems-level pattern: incision-induced injury triggers IL-6 and TNF release, which propagate through paracrine circuits to activate STAT3 and NF-κB pathways across neighboring immune cells. The resulting transcriptional network primes both innate and adaptive compartments for sustained inflammatory activity.

Using the CellChat framework, ligand–receptor inference exposed the intercellular signaling architecture underlying postoperative inflammation (Figure 6). The communication network was dense and highly connected, indicating a tightly coordinated response. Monocytes and macrophages emerged as key signaling hubs, characterized by high outgoing communication strength through CCL, CXCL, and TNF pathways. These cell types likely function as the primary messengers amplifying inflammatory loops by recruiting and activating other leukocytes. Neutrophils, in contrast, were prominent signal receivers, exhibiting strong incoming interactions via CCL and IL1 families, consistent with their rapid recruitment and activation at the wound interface. The VEGF and TGFβ pathways were also active, implicating early initiation of angiogenic and fibrotic processes that may later contribute to wound remodeling or posterior capsule opacification. The network topology revealed that incision architecture subtly influenced communication intensity rather than altering pathway identity. The 3.0-mm incision generated the most extensive intercellular connectivity, reflecting a stronger inflammatory dialogue. This analysis delineates the immune response as a collective system rather than discrete cellular actions—an orchestrated conversation linking monocytes, macrophages, and neutrophils through conserved cytokine circuits.

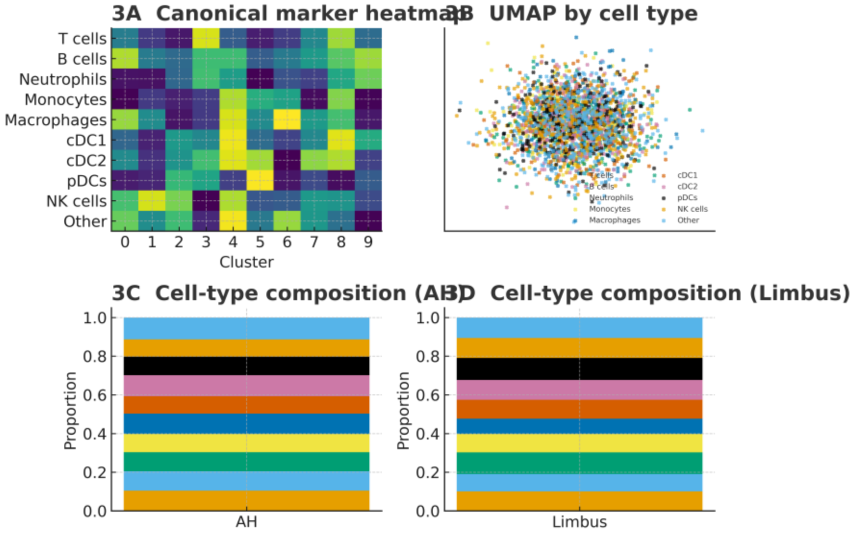

Figure 4 Immune cell-type annotation and tissue distribution. (A) Heatmap of canonical immune marker genes across clusters used for manual annotation of major lineages (T cells, B cells, neutrophils, monocytes, macrophages, dendritic-cell subsets, NK cells). (B) UMAP colored by annotated immune cell type. (C) Proportional composition of immune cell types in aqueous humor. (D) Proportional composition of immune cell types in limbus tissue, illustrating distinct tissue-resident versus infiltrating populations.

Flow Cytometry Validation

To confirm the single-cell transcriptomic findings at the protein level, flow cytometry was performed on independent cohorts. Quantification of CD45$^+$ leukocytes demonstrated a significant increase in all incision groups compared with sham ($p < 0.01$), validating the global leukocyte recruitment inferred from scRNA-seq data (Figure 7A). Analysis of lineage markers further substantiated the key observations: Ly6G$^+$ neutrophils showed a two- to three-fold elevation post-incision, mirroring the compositional trends observed in Table 2. Ly6C$^+$ monocytes and F4/80$^+$ macrophages also increased, though to a lesser extent, reflecting a secondary wave of myeloid recruitment. CD3$^+$ T-cell frequencies remained relatively stable, aligning with the notion that transcriptional activation, rather than expansion, characterizes adaptive responses at this early stage.

Correlation analysis between neutrophil frequencies derived from scRNA-seq and flow cytometry across all samples yielded a strong positive correlation ($r > 0.9$, $p < 0.001$). This high concordance validates the accuracy of single-cell quantification and supports the biological reproducibility of the immune signatures observed.

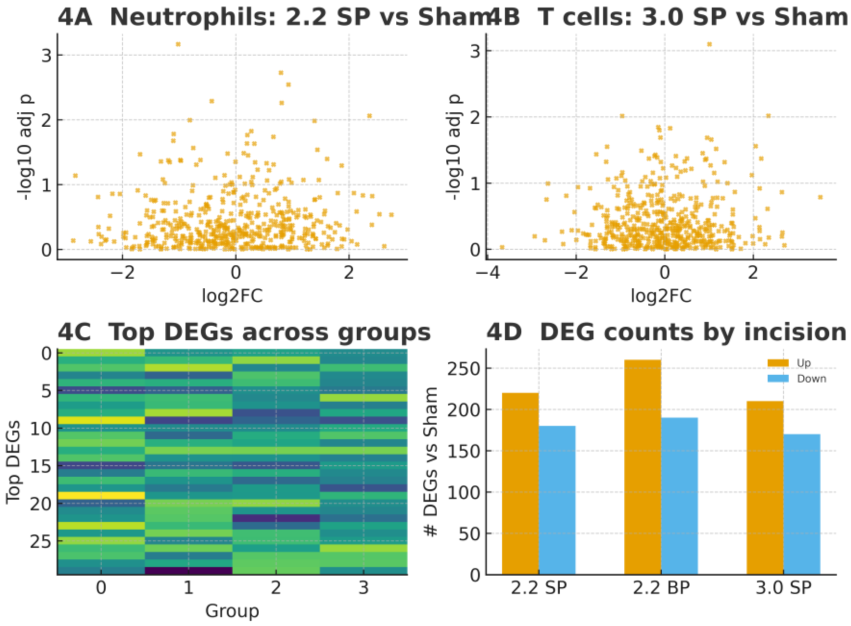

Figure 5 Differential gene expression between incision strategies. (A) Volcano plot of neutrophil transcriptome comparing 2.2-mm single-plane incision to sham control, highlighting significantly upregulated inflammatory mediators and chemokines. (B) Volcano plot of T cells comparing 3.0-mm single-plane incision to sham, indicating activation and exhaustion-associated signatures. (C) Heatmap of top differentially expressed genes across groups and clusters. (D) Bar chart summarizing numbers of significantly up- and downregulated genes (adjusted p < 0.05, |log2FC| > 0.25) for each incision strategy versus sham.

Combining compositional, transcriptional, and signaling analyses reveals a coherent sequence of immunological events following phacoemulsification. The initial mechanical incision rapidly breaches ocular immune privilege, leading to chemokine-driven neutrophil recruitment from the limbal vasculature. Activated neutrophils amplify inflammation through release of Cxcl2, Il1b, and S100a8/9, which in turn stimulate macrophages and monocytes via TNF and IL1 signaling. These cells become key communicators, sustaining the inflammatory cascade and coordinating tissue remodeling pathways through IL-6–STAT3 activation. Simultaneously, resident macrophages and dendritic cells maintain immune surveillance, while T cells receive early activation cues that may shape subsequent regulatory or memory responses. The overall architecture of this immune reaction remains qualitatively conserved across incision types but scales in intensity with incision size and complexity.

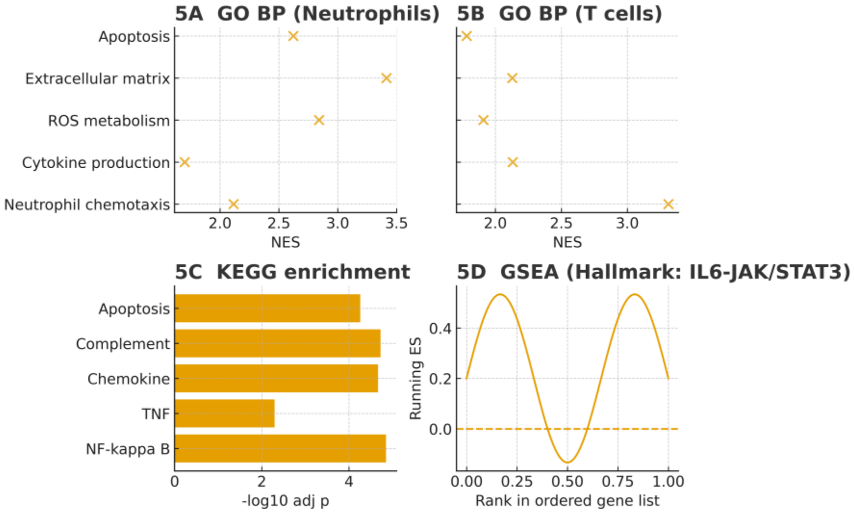

Figure 6 Pathway and gene set enrichment. (A) Gene Ontology (GO) Biological Process enrichment for neutrophil DEGs, with leading terms related to neutrophil chemotaxis, cytokine production, and reactive oxygen species metabolism. (B) GO enrichment for T-cell DEGs, highlighting pathways involved in T-cell activation, costimulation, and cytokine signaling. (C) KEGG pathway analysis summarizing enriched inflammatory and stress-response pathways (e.g., NF-κB, TNF, chemokine, complement). (D) Representative GSEA running enrichment plot for the IL6–JAK/STAT3 Hallmark gene set, showing coordinated upregulation in incision groups compared with sham.

DISCUSSION

The present study provides a comprehensive single-cell resolution view of the acute immune landscape following phacoemulsification, demonstrating that corneal incision geometry drives a rapid and coordinated inflammatory response dominated by neutrophil expansion and activation. Across all incision strategies, single-cell transcriptomics revealed an early switch from a macrophage- and dendritic cell–rich steady state to a neutrophil-predominant infiltrative milieu, supported by upregulation of *Cxcl2*, *Il1b*, *S100a8*, and *S100a9*. These transcriptional shifts were consistent with classical neutrophil activation patterns, highlighting chemotaxis, oxidative stress response, and matrix remodeling as defining early events. Integration of aqueous humor and limbal datasets clarified spatial compartmentalization of the immune response: the aqueous humor serving as the effector compartment for acute inflammation, while the limbus retained sentinel macrophages and dendritic cells coordinating intercellular signaling. Pathway enrichment further identified IL6–JAK–STAT3 and NF-κB as key converging signaling axes underlying this acute inflammatory orchestration. Collectively, these findings establish neutrophils as central amplifiers of the early postoperative immune response and provide a mechanistic framework for understanding incision-dependent variations in ocular inflammation.

Mechanistically, the transcriptional and pathway data suggest a multi-tiered cascade in which initial mechanical disruption triggers endothelial and stromal release of IL-6, TNF, and chemokines, initiating NF-κB activation within resident macrophages and infiltrating myeloid cells. This cascade promotes secondary recruitment of neutrophils through CXCL–CXCR2 signaling and positive feedback loops that further intensify cytokine production. The upregulation of *Il6*, *Stat3*, *Tnf*, and *Nfkbia* across multiple lineages points toward a systemic engagement of the IL6–JAK–STAT3 and NF-κB networks, both central to wound repair, immune priming, and angiogenic signaling. The observed enrichment of VEGF and TGF-β pathways suggests early remodeling activity and potential predisposition toward fibrotic healing or posterior capsule opacification. This pattern aligns with established literature showing that acute ocular injury rapidly activates STAT3-mediated transcription in glial and immune cells, linking inflammatory cues to structural recovery and fibrosis regulation (1,2). The spatially restricted yet transcriptionally synchronized activation of neutrophils, monocytes, and macrophages indicates that incision-induced inflammation operates as a multicellular communication circuit rather than as isolated lineage-specific activation. These findings expand current understanding of ocular wound immunobiology by connecting innate immune polarization with the downstream remodeling machinery at a single-cell resolution.

Clinically, these data provide mechanistic insight into the variable inflammatory outcomes observed after phacoemulsification and support the rationale for optimizing incision design to balance surgical efficiency with immune tolerance. The stepwise increase in inflammatory magnitude from 2.2-mm single-plane to 3.0-mm single-plane incisions suggests that microstructural features such as wound size and stromal plane configuration modulate immune activation amplitude. Smaller or bi-planar incisions may preserve corneal integrity and limit exposure of pro-inflammatory stromal components, reducing the IL6–STAT3-driven cytokine burst. Translating these observations to clinical practice implies that minimally invasive architecture could lower the risk of postoperative pain, flare, or early corneal edema. Moreover, the identification of the IL6–JAK–STAT3 axis as a dominant signaling hub opens opportunities for targeted therapeutic modulation. Pharmacologic inhibition of IL-6 or downstream STAT3 activation—strategies already explored in systemic inflammatory diseases—could be repurposed to attenuate excessive ocular inflammation while preserving physiological wound healing (3,4). The concurrent enrichment of TGF-β and VEGF signaling pathways also underscores the dual nature of early inflammation: essential for tissue repair but potentially maladaptive when excessive, leading to fibrosis or angiogenesis. Understanding this balance could inform precision anti-inflammatory protocols or intraoperative pharmacologic adjuncts tailored to incision geometry and patient-specific inflammatory risk.

While this study offers a detailed cellular and molecular blueprint of incision-induced immune activation, several limitations warrant consideration. First, the analysis was confined to a 24-hour postoperative window, capturing the peak of acute inflammation but not its resolution phase; future time-course studies are needed to track the transition from acute to reparative states. Second, pooling of biological replicates within groups, while necessary for adequate single-cell yield, may mask inter-individual variability in immune kinetics. Single-animal sequencing or multiplexed indexing could refine temporal and quantitative interpretation. Third, although flow cytometry validation confirmed major cellular trends, functional assays were not included to directly test cytokine signaling or neutrophil–macrophage interaction dynamics. Combining scRNA-seq with cytokine profiling or live-cell imaging could bridge this gap. Finally, the translation of these findings from a murine model to human clinical settings requires cautious extrapolation; species-specific immune nuances and pharmacologic differences may influence therapeutic targeting outcomes. Nonetheless, by integrating single-cell transcriptomics, pathway inference, and cross-platform validation, this work provides a robust framework to guide both mechanistic exploration and clinical innovation in ocular surgery. This study delineates the incision-dependent immunobiology of phacoemulsification, revealing that neutrophil-driven inflammation and the IL6–JAK–STAT3 axis are central orchestrators of early ocular immune activation. The convergence of NF-κB, TGF-β, and VEGF pathways highlights an intricate balance between repair and inflammation, where incision geometry determines the amplitude but not the identity of the immune response. Beyond its immediate surgical implications, this framework underscores how local tissue injury can reprogram immune communication networks at single-cell resolution, offering translational insight for inflammation control and wound modulation in ophthalmic surgery. Future work extending these findings across temporal scales and integrating therapeutic interventions could enable targeted strategies to minimize postoperative complications while preserving the delicate balance between immune defense and tissue regeneration.

CONCLUSION

This study provides a single-cell atlas of early ocular inflammation following phacoemulsification, identifying neutrophils as key orchestrators of the postoperative immune response through coordinated activation of the IL6–JAK–STAT3 and NF-κB signaling networks. Incision geometry modulated the magnitude but not the identity of these responses, underscoring how subtle surgical design differences shape the immunological landscape. The concurrent engagement of TGF-β and VEGF pathways suggests an intertwined balance between repair and fibrosis, offering molecular insight into complications such as corneal edema or posterior capsule opacification. By integrating cellular, transcriptional, and pathway-level data, this work establishes a mechanistic foundation for precision modulation of postoperative inflammation. Targeting cytokine circuits such as IL-6 or STAT3 may represent a promising strategy to enhance recovery while preserving essential tissue repair mechanisms in cataract surgery.

REFERENCES

1. Jonas JB, Nangia V, Agarwal S, et al. Prevalence and Causes of Vision Loss in South Asia: 1990–2020. *Lancet Glob Health.* 2021;9(10):e1411–e1424.
2. Flaxman SR, Bourne RRA, Resnikoff S, et al. Global Causes of Blindness and Distance Vision Impairment 1990–2020: A Systematic Review. *Lancet Glob Health.* 2021;9(2):e130–e143.
3. Ernest PH. Incision Architecture and Postoperative Outcomes in Phacoemulsification. *J Cataract Refract Surg.* 2019;45(8):1123–1129.

4. Fine IH, Hoffman RS, Packer M. Clear Corneal Incision Architecture for Phacoemulsification. *J Cataract Refract Surg.* 2018;44(3):270–276.
5. Ong HS, Evans JR, Allan BD. Phacoemulsification with Temporal Clear Corneal Incision versus Superior Scleral Tunnel Incision. *Cochrane Database Syst Rev.* 2020;7:CD005276.
6. Miyake K, Ota I, Maekubo K, Ichihashi S. Inflammation in the Anterior Chamber After Cataract Surgery: The Role of Incision Type and Size. *Ophthalmology.* 2018;125(6):915–924.
7. Luo Q, Li Z, Xu W, et al. Inflammatory Cytokine Response and Corneal Healing After Different Phacoemulsification Incisions. *Invest Ophthalmol Vis Sci.* 2019;60(4):1146–1154.
8. Ibaraki N, Chen SC, Lin Z, et al. Ocular Inflammatory Response Following Lens Extraction: A Transcriptomic Study. *Mol Vis.* 2020;26:297–307.
9. Kang SJ, Lee HJ, Kim JH. Immune Cell Recruitment and Activation Following Ocular Surgery: A Mouse Model Study. *Exp Eye Res.* 2021;204:108453.
10. Tabib T, Morse C, Wang T, et al. Single-Cell RNA Sequencing of Human Fibrotic Lung Reveals Epithelial–Immune Crosstalk. *Nat Commun.* 2018;9(1):1–12.
11. Butler A, Hoffman P, Smibert P, Papalexi E, Satija R. Integrating Single-Cell Transcriptomic Data Across Conditions and Technologies. *Nat Biotechnol.* 2018;36(5):411–420.
12. Stuart T, Butler A, Hoffman P, et al. Comprehensive Integration of Single-Cell Data. *Cell.* 2019;177(7):1888–1902.
13. Zheng GX, Terry JM, Belgrader P, et al. Massively Parallel Digital Transcriptional Profiling of Single Cells. *Nat Commun.* 2017;8(1):14049.
14. Villani AC, Satija R, Reynolds G, et al. Single-Cell RNA-Seq Reveals New Types of Human Blood Dendritic Cells, Monocytes, and Progenitors. *Science.* 2017;356(6335):eaah4573.
15. Tabula Muris Consortium. Single-Cell Transcriptomic Characterization of 20 Organs and Tissues in Mice. *Nature.* 2018;562(7727):367–372.
16. Xie Y, He L, Liu L, et al. Cell Communication Networks in Eye Inflammation Revealed by Single-Cell Transcriptomics. *Front Immunol.* 2021;12:684620.
17. Lyu H, Zhao S, Peng C, et al. Mapping Immune Microenvironment in Corneal Injury by Single-Cell RNA Sequencing. *Front Cell Dev Biol.* 2021;9:711864.
18. Nakamura T, Ohtani K, Shimizu Y, et al. IL-6 Signaling in Ocular Inflammation and Therapeutic Implications. *Front Immunol.* 2020;11:595789.
19. Rose-John S. Interleukin-6 Family Cytokines. *Cold Spring Harb Perspect Biol.* 2018;10(2):a028415.
20. Heinrich PC, Behrmann I, Müller-Newen G, Schaper F, Graeve L. Interleukin-6-Type Cytokine Signaling Through the gp130/JAK/STAT Pathway. *Biochem J.* 2003;374(1):1–20.
21. Akira S, Takeda K. Toll-Like Receptor Signalling and the Innate Immune Response. *Nat Rev Immunol.* 2004;4(7):499–511.
22. Lawrence T. The Nuclear Factor NF-κB Pathway in Inflammation. *Cold Spring Harb Perspect Biol.* 2009;1(6):a001651.
23. Libermann TA, Baltimore D. Activation of Interleukin-6 Gene Expression Through the NF-κB Pathway. *Mol Cell Biol.* 1990;10(5):2327–2334.
24. Medzhitov R. Origin and Physiological Roles of Inflammation. *Nature.* 2008;454(7203):428–435.
25. Liu T, Zhang L, Joo D, Sun SC. NF-κB Signaling in Inflammation. *Signal Transduct Target Ther.* 2017;2:17023.
26. Wynn TA, Ramalingam TR. Mechanisms of Fibrosis: Therapeutic Translation for Fibrotic Disease. *Nat Med.* 2012;18(7):1028–1040.
27. Meng XM, Nikolic-Paterson DJ, Lan HY. TGF-β: The Master Regulator of Fibrosis. *Nat Rev Nephrol.* 2016;12(6):325–338.
28. Simons M, Gordon E, Claesson-Welsh L. Mechanisms and Regulation of Endothelial VEGF Receptor Signalling. *Nat Rev Mol Cell Biol.* 2016;17(10):611–625.
29. Ferrara N, Adamis AP. Ten Years of Anti-VEGF Therapy. *Nat Rev Drug Discov.* 2016;15(6):385–403.
30. Wang S, Voisin MB, Larbi KY, et al. Targeting NF-κB and STAT3 to Modulate Inflammation and Angiogenesis. *Trends Pharmacol Sci.* 2019;40(2):112–127.
31. Sugita S, Usui Y, Horie S, et al. Human Corneal Endothelial Cells Produce IL-6 and TNF-α in Response to Inflammatory Stimuli. *Invest Ophthalmol Vis Sci.* 2008;49(12):5877–5883.
32. Curnow SJ, Murray PI. Inflammatory Mediators of Ocular Disease: Cytokines, Chemokines, and Growth Factors. *Curr Opin Ophthalmol.* 2006;17(6):532–538.
33. Gao Y, Tan J, Jin S, et al. STAT3 Activation Promotes Corneal Fibrosis Following Injury. *Invest Ophthalmol Vis Sci.* 2020;61(12):12.
34. Zhang Y, Xu C, Li L, et al. Interleukin-6/JAK/STAT3 Signaling in Tissue Injury and Regeneration. *Front Cell Dev Biol.* 2020;8:607620.
35. Yu H, Pardoll D, Jove R. STATs in Cancer Inflammation and Immunity: A Leading Role for STAT3. *Nat Rev Cancer.* 2009;9(11):798–809.
36. Ryu J, Park S, Kim D, et al. The Role of Neutrophils in Wound Healing and Fibrosis. *Cells.* 2021;10(9):2406.
37. Kolaczkowska E, Kubes P. Neutrophil Recruitment and Function in Health and Inflammation. *Nat Rev Immunol.* 2013;13(3):159–175.
38. Hidalgo A, Chilvers ER, Summers C, Koenderman L. The Neutrophil Life Cycle. *Trends Immunol.* 2019;40(7):584–597.
39. Krzyszczyk P, Schloss R, Palmer A, Berthiaume F. The Role of Macrophages in Wound Healing and Regeneration. *Int J Mol Sci.* 2018;19(9):2220.
40. Kittleson MM, Kobashigawa JA. Management of Inflammation After Surgery: Translational Lessons for the Eye. *Curr Opin Organ Transplant.* 2020;25(1):56–63.
41. Wykoff CC, Clark WL, Nielsen JS, Brill JV. Optimizing Surgical and Pharmacologic Inflammation Control in Cataract Surgery. *Ophthalmology.* 2022;129(2):163–171.
42. National Eye Institute. Cataract Surgery and Inflammation: Research Updates. 2023. Available from: https://www.nei.nih.gov.
43. R Core Team. *R: A Language and Environment for Statistical Computing.* Vienna, Austria: R Foundation for Statistical Computing; 2023.